Tailoring grain growth and densification toward a high-performance solid-state electrolyte membrane

Min Hong [1,†], Qi Dong [1,†], Hua Xie [1,†], Xizheng Wang [1], Alexandra H. Brozena [1], Jinlong Gao [1], Chengwei Wang [1], Chaoji Chen [1], Jiancun Rao [4], Jian Luo [2], Liangbing Hu [1,3,*]

[1] Department of Materials Science and Engineering, University of Maryland, College Park, MD 20742, United States
[2] Department of NanoEngineering, University of California, San Diego, La Jolla, CA 92093, United States
[3] Center for Materials Innovations, University of Maryland, College Park, MD 20742, United States
[4] Advanced Imaging and Microscopy Laboratory, University of Maryland, College Park, MD 20742, United States

The synthesis of dense and uniform solid-state electrolyte membranes for Li batteries is challenging due to the lack of fine control over the grain growth by conventional sintering methods. Using such techniques, abnormal grain growth can often occur, with associated contaminants and voids, often resulting in electrolyte membranes that suffer from high resistivity, poor stability, and the risk of Li dendrite penetration. Herein, we report a new high-temperature (1500 K) and rapid sintering (30 s) process by Joule heating that tailors the grain growth and densification toward high-quality, high-performance solid-state electrolyte membranes. The high temperature contributes to the rapid removal of impurities, leading to a dense and uniform microstructure in seconds. The short sintering time provides controlled grain growth, with nearly unchanged grain size and distribution compared to the solid-state electrolyte powders prior to sintering. Using calcined Ta-doped $Li_7La_3Zr_2O_{12}$ (LLZTO) garnet powders, we show that the grain size distribution before and after the rapid sintering are nearly identical (~4 μm for both), while defects (*e.g.*, voids and gaps) and impurities are effectively eliminated. The resulting high-quality membrane features good ionic conductivity (6.4×10^{-4} S cm^{-1} at room temperature) and excellent stability during lithium striping/plating (>300 h under 0.2 mA cm^{-2}), making it suitable for Li battery applications. This high-temperature rapid sintering approach can be further extended to a variety of ceramic Li^+ conductors toward the future development of solid-state batteries.

Introduction

Solid-state electrolyte holds great potential to improve the energy density and safety of future Li batteries [1,2]. Among the various solid-state electrolyte candidates, ceramic Li^+ conductors stand out due to their high conductivity, good mechanical strength, and wide electrochemical window [3–6]. Great attention has thus been paid to the synthesis of solid ceramic membranes [4–7], which are generally made by conventional sintering techniques that feature long sintering times (*e.g.*, 10 h), mild-temperatures (~1300 K), slow heating rates (*e.g.*, 10 K/min), and/or high pressure (*e.g.*, 50 MPa) [8–11]. Microscopically, these conventional sintering approaches often generate voids and contaminants in the membrane, which lead to high resistivity as well as poor safety due to the Li dendrite penetration [12–19]. Inhomogeneous elemental distribution from

---

* Corresponding author.

E-mail address: Hu, L. (binghu@umd.edu)

† These authors contributed equally.

1369-7021/© 2020 Elsevier Ltd. All rights reserved. https://doi.org/10.1016/j.mattod.2020.10.002

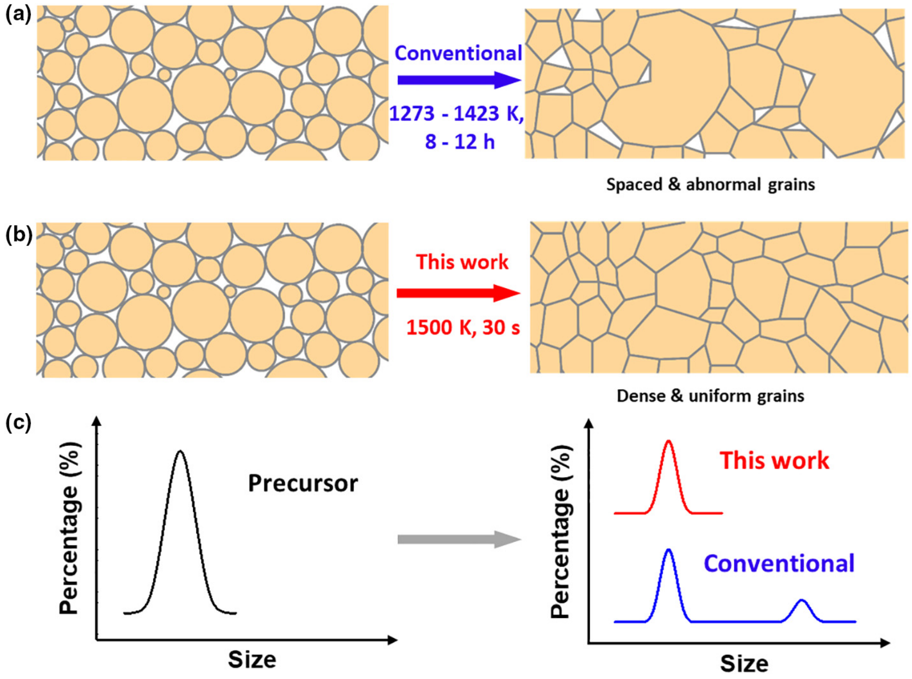

FIGURE 1

Schematic comparison between conventional methods and our high-temperature rapid sintering of ceramic solid-state electrolyte synthesis. (a) Conventional approaches feature long synthesis time, leading to a wide particle size distribution and large amounts of voids and gaps. (b) The high-temperature rapid sintering method features a significantly reduced synthesis time, from hours to seconds, resulting in uniform grain size distribution and a dense microstructure of the sintered membrane. (c) Schematic illustration of the particle size distribution before and after sintering by conventional methods and the high-temperature rapid sintering technique.

uncontrolled grain growth can also deteriorate the electrochemical performance [16,19]. Furthermore, the long sintering duration often requires a large amount of extra protective precursor powder (bed powder) for the pellet to prevent Li loss. Most importantly, conventional sintering offers limited control over the crystal coarsening process, in which abnormal grain growth and varying size distributions can create critical issues [20–24]. Although many studies have shown that the reduced grain size and its uniform distribution contribute to high mechanical strength [25], optimal homogeneity [26–28], and good air stability [21,29], it remains challenging to have this level of control by conventional sintering methods. As a result, these issues have hindered the development of solid-state electrolyte for practical applications [30–33].

Results and discussion

Herein, we report a new method by Joule heating at a high temperature (1500 K) for the rapid synthesis (seconds instead of hours) of high-quality membranes from solid-state electrolyte powders. Carbon felt was used as the Joule heating element for highly efficient sintering where temperature and heating duration can be accurately tuned by adjusting the electric power input. Fig. 1a and b schematically compares conventional methods with our high-temperature rapid sintering approach for synthesizing solid-state electrolyte membranes. During the long process (*e.g.*, under 1273–1423 K for 8–12 h, Fig. 1a) of conventional sintering, the evolution of gas and voids often occur [8,9,12,16–19]. This lack of fine control over the grain growth process results in wide or even bi-modal particle size distribution (abnormal grain growth) (Fig. 1c) [8,12,19]. In comparison, our high-temperature rapid sintering method (Fig. 1b) allows for well-controlled grain boundaries and uniform grain size that are nearly identical to that of the calcined solid-state electrolyte powders. Additionally, voids can be effectively eliminated upon sintering, enabling a highly uniform and dense microstructure to be obtained. Note that there are no gaseous products during sintering in our process which employs solid-state electrolyte powders as opposed to the reactive sintering. This feature of our process also benefits in the dense structure and well-controlled grain growth. Compared to the membranes made by conventional methods, the resulting solid-state electrolyte membrane prepared by this high-temperature rapid sintering process is expected to have better electrochemical performance. This technique can be used to tailor the grain growth and densification for a range of solid-state electrolytes to support the development of future solid-state batteries.

To demonstrate this high-temperature rapid sintering process, we synthesized Ta-doped $Li_7La_3Zr_2O_{12}$ (LLZTO) as a model solid Li^+ conductor that features a garnet structure. Two pieces of carbon felt, which served as the Joule heating elements, were sandwiched around a pressed pellet made of calcined LLZTO powders (Fig. 2a). In a typical sintering process, we applied a current to the carbon felt in order to ramp its temperature up to 1500 K within ~1 s via Joule heating, as measured by a thermal sensing camera (Fig. 2a and Fig. S1). After holding at a constant temperature for 30 s, the temperature of the carbon felt heater was

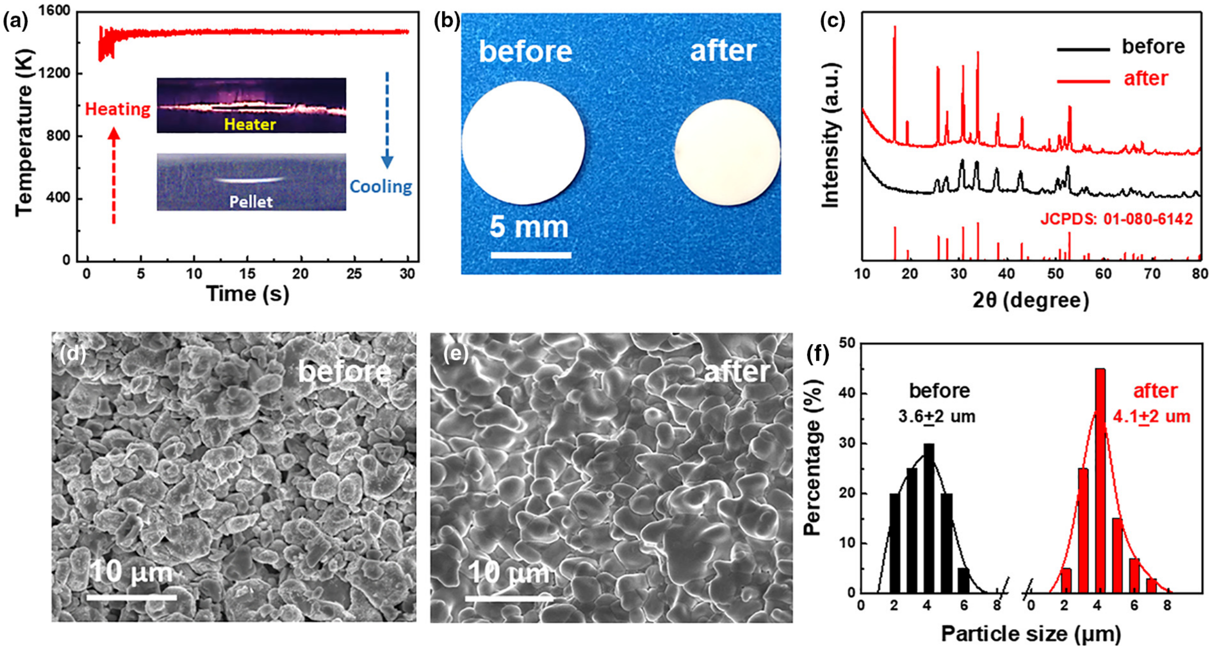

FIGURE 2

(a) Temperature profile of the high-temperature rapid sintering method. The inset images show an LLZTO pellet sandwiched between the carbon felt Joule heaters before (bottom) and during sintering (top). (b) Digital image comparing the LLZTO membrane before and after the high-temperature rapid sintering process. (c) XRD analysis of the pressed pellet made of calcined LLZTO powders and the sintered membrane, in comparison to the standard diffraction pattern of $Li_{6.5}La_3Zr_{1.45}Ta_{0.55}O_{12}$ (JCPDS: 01-080-6142). (d and e) Surface microstructure of the LLZTO membrane (d) before and (e) after high-temperature rapid sintering. (f) Statistical analysis of the grain size and distribution based on the SEM images before and after the high-temperature rapid sintering process.

cooled down to room temperature (298 K) in less than 1 s by simply turning off the applied current. Digital image of the membrane before and after high-temperature rapid sintering reveals a slight decrease of the membrane diameter by ~12.5%, which is moderate compared with the literature (Fig. 2b) [11]. For a typical sample, after sintering, the thickness of the membrane decreased from ~562 μm to ~418 μm meanwhile the membrane remained flat without deformation. In practice, less size change is desired for scalable production and quality control, which has been a major challenge for conventional methods [11].

We characterized the resulting material to verify its composition and morphology. Fig. 2c shows the X-ray diffraction (XRD) pattern of the sintered LLZTO membrane matches well with the standard pattern of cubic phase $Li_{6.5}La_3Zr_{1.45}Ta_{0.55}O_{12}$ (JCPDS: 01-080-6142). Additionally, the sharp and clean diffraction pattern indicates good crystallinity and high purity of the whole membrane. Surface microstructure of the pressed pellet made of calcined LLZTO powders and the sintered membrane are shown by scanning electron microscopy (SEM) images in Fig. 2d and Fig. 2e, respectively. Before the high-temperature sintering, the LLZTO powders (in the form of micron-size particles) were uniform but with some agglomeration, demonstrating a mean size of ~3.6 μm (Fig. 2f). SEM images at higher magnitude demonstrate a rough morphology due to the presence of impurities on the surface, such as lithium oxide and lithium carbonate (Fig. S2A, B) [34]. After high-temperature sintering, the particles become fused together, forming a dense and pinhole-free microstructure (Fig. 2e). The mean size of the grains on the surface of the sintered membrane was ~4.1 μm with slightly narrower size distribution than before (Fig. 2f), which are consistent with the fractured cross-sections (~4.5 μm) (Fig. S2). In addition, the high temperature quickly removed the impurities as verified by Raman spectroscopy (Fig. S3) and led to the clean boundaries of the sintered grains (Fig. 2e). The absence of contamination in part contributed to the formation of well-merged grain boundaries (Fig. S2C, D). Moreover, the fractured cross-sections illustrate a trans-granular fracture mode, which indicates strong grain boundaries and high mechanical strength of the sintered membrane (Fig. S2E, F).

We also tracked the morphological evolution of the membrane at 15 s intervals over a total of 60 s sintering at 1500 K using SEM to better understand the grain growth process (Fig. 3a and Fig. 3b). The pellets made of calcined LLZTO powders showed a mean grain size of 3.6 μm and featured a rough surface (Fig. 3b). After the first 15 s of sintering, the surface of the grains turned smooth and clean, indicating this amount of time was sufficient to remove the impurities by the high-temperature. During this time, the LLZTO particles also began to connect to each other by "neck growth," which is controlled by the surface diffusion [19]. During this stage, the grain boundaries began to form and grow with the driving force of surface energy. However, the grain size only increased marginally to 3.8 μm (Fig. 3c) without completely filling the voids and gaps (Fig. 3b). The relative density of the LLZTO membrane also only slightly increased from 50% to 68.2% at this stage (Fig. 3d). After sintering for 30 s at the same temperature, the membrane became denser and pinhole-free. In this second period (15–30 s), more atoms diffuse to the "neck" area, leading to the complete removal of

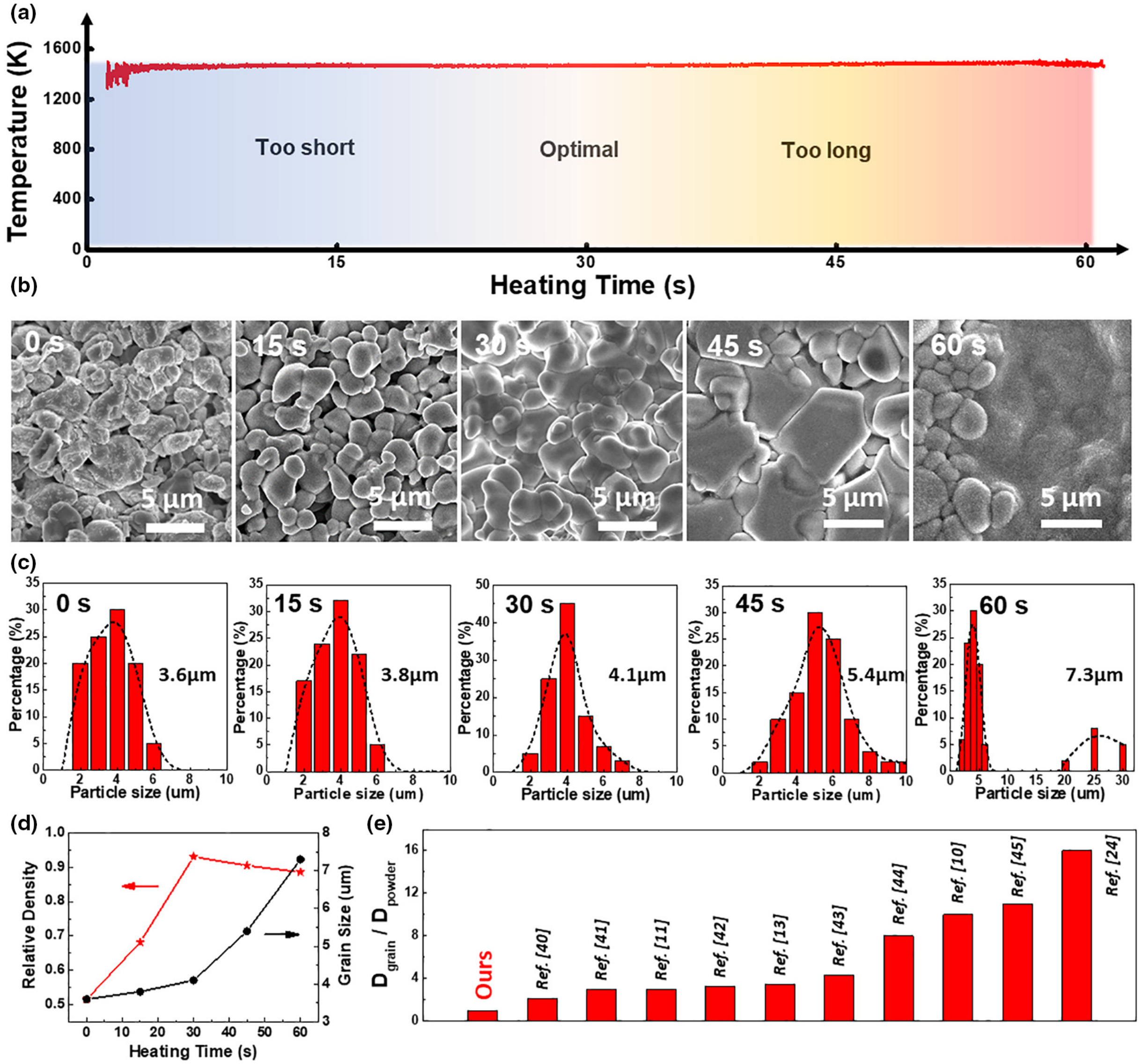

FIGURE 3

(a) Temperature profile of the high-temperature rapid sintering method. (b) SEM images showcasing the surface microstructures of the pellet made of calcined LLZTO powders and after each 15 seconds of the entire 60 s sintering process. (c) Statistical analysis of the grain size and distribution of the LLZTO membrane based on the SEM images at each time point during the total sintering process. (d) Relative density and average grain size of the LLZTO membrane at each time point during the sintering process. (e) Comparison between the literature and our approach on the size ratio of the grains (D_{grain}) from the sintered membrane to the calcined powders (D_{powder}).[10,11,19,21,40–45].

pores (Fig. 3b) [35,36]. Surface tension is the key driving force for the densification during this period, with the surface energy drastically decreased due to the elimination of voids [37,38]. The mean grain size increased to 4.1 µm while the relative density increased to 93.1% (Fig. 3c, d). Additionally, at this stage, the smooth and clean surfaces are preserved on the fused grains (Fig. S4). The fractured cross-sectional SEM images of the membrane at this stage show a trans-granular mode also with clean boundaries (Fig. S5).

However, longer sintering resulted in further grain growth that was less uniform. After 45 s of heating at 1500 K, the merged grains have enough time to diffuse and grow so that some of the grain boundaries completely disappeared (Fig. 3b). In this third period (30–45 s), driven by surface energy, the smaller grains tend to be gradually overtaken by the growth of larger grains, following an Ostwald ripening mechanism [39]. Note that SEM images with lower magnification (Fig. S6) were used for statistical analyses since the grain size distribution changed more dramatically at this stage. The mean grain size increased to 5.4 µm along with a much broader distribution compared to the previous stages (Fig. 3c), while the density slightly decreased to 90.5% compared to the 30 s sintered sample (Fig. 3d). After 60 s of sintering, abnormal grain growth occurred, possibly due to secondary recrystallization or the decomposition of LLZTO (Fig. 3b). The dramatic change of the microstructure also resulted in the slight bending of the membrane (Fig. S7A), which is undesirable for practical applications as a solid-state electrolyte. Some of the grain boundaries also disappeared, in which extremely large grain were formed, surrounding smaller grains in an abnormal structure (Fig. S7B, C). The mean grain size was measured to be ~7.3 μm with a bi-modal distribution (Fig. 3c). Meanwhile, the relative density of the LLZTO membrane further decreased to 88.6% (Fig. 3d). The decrease of the relative density may be due to Li loss and/or recrystallization of the LLZTO membrane. This abnormal growth and possible decomposition of the LLZTO membrane further created new voids and gaps (Fig. 3b). These results indicate that 30 s of sintering is optimal in terms of membrane quality. The grain size evolution of the LLZTO membrane was also studied using the fractured cross-sectional SEM images (Fig S8), which demonstrates nearly identical trend with that of the surface grains. Under this condition, our high-temperature rapid sintering process offers better control in grain growth with limited increase of grain size after sintering (Fig. 3e) [10,11,19,21,40–45].

To ensure the uniformity of the synthesized membrane, we characterized the surface morphology of the membrane by SEM (Fig. 4a). No obvious voids or gaps were observed throughout the whole surface. To confirm the material's good uniformity, we also collected SEM images at higher magnification at three representative regions of the membrane surface. Nearly identical morphologies were observed for all three areas (Fig. 4b), as well as at other spots of the membrane, which featured an almost identical microstructure and grain size distribution (Fig. S9). The average diameter of the grain was ~4.1 μm, agreeing with the results presented in Fig. 3. The surfaces of the grain at the three spots also appeared smooth and clean. The cross-sectional SEM image from the fractured membrane was also presented that verifies the uniformity (Fig. S10A). A typical trans-granular fracture mode together with uniform grain size and clean grain boundaries confirm the high quality of the membrane (Fig. S10B and Fig. S11). These features are critical to enable high performance of the solid-state electrolyte in Li battery applications.

To evaluate the electrochemical performance, we fabricated a Li|LLZTO membrane|Li symmetric cell using a sintered LLZTO membrane prepared under the optimal conditions of 1500 K for 30 s. A galvanostatic cycling test using the symmetric cell demonstrated the stable operation of the sintered LLZTO membrane up to 300 h at a current density of 0.2 mA cm^{-2} without shorting or any abnormal polarizations (Fig. 4c). Electrochemical impedance spectroscopy (EIS) revealed a low areal specific resistance of 60 Ω cm^2 and an ionic conductivity of 6.4×10^{-4} S cm^{-1} at 298 K, with the former being among the best reported in the literature (Fig. 4d) [8,11,12–14,21,33,34,45–49]. We calculated the activation energy (E_a) for Li^+ conduction to be only 0.33 eV according to the Arrhenius equation, $\sigma T\ \exp(-E_a/KT)$, as measured in the range from 298 K to 383 K (Fig. 4e). The high conductivity and low activation energy can be attributed to the uniform, dense, and impurity-free microstructure. As we increased the current density from 0.1 mA cm^{-2} to 0.65 mA cm^{-2}, we did not observe any instability in the cycling performance, indicating the membrane's good rate capability (Fig. 4f). Additional cycling tests using an areal capacity of 0.1 mAh cm^{-2} with 0.1 mA cm^{-2} and 0.2 mA cm^{-2} also demonstrated stable performance (Fig. S12). When comparing with a range of garnet $Li_7La_3Zr_2O_{12}$ (LLZO)-based solid-state electrolytes prepared by other methods (including LLZTO), our material represents the high end of the products in terms of its controlled grain size, uniform and dense structure, rapid processing, and good electrochemical performance (Table S1).

Our method can be readily expanded from garnet-type solid-state Li^+ conductors to a variety of other materials. To demonstrate the broad applicability of our technique, we applied the same synthetic process on another model solid-state electrolyte of $Li_{0.348}La_{0.55}TiO_3$ (LLTO), which has a perovskite structure. An image of the LLTO membrane before and after the high-temperature sintering process reveals a ~17% decrease in diameter (Fig. 5a), similar to that observed for LLZTO. Note that the color of LLTO membrane changed from white (in the precursor state) to grey (in the sintered state), which we attribute to the reduction of Ti^{4+} to Ti^{3+} at temperatures higher than 1173 K in an inert atmosphere [50]. After high-temperature sintering at 1500 K for 30 seconds, the separated powders (in the form of particles, Fig. S13) merged together to form a dense and uniform structure (Fig. 5b). The XRD diffraction pattern of LLTO membrane (Fig. S14) that matches well with standard $Li_{0.3}La_{0.567}TiO_3$ structure confirms its high purity and good crystallinity. The particles became well interconnected and pores were completely eliminated. Macroscopically the membrane remained flat without any deformation, such as bending or humping, which is consistent with the LLZTO case. We measured the ionic conductivity of sintered LLTO membrane to be 1.4×10^{-3} S cm^{-1} at 298 K according to the fitted EIS curve with equivalent circuit corresponding to a Li|PEO|LLTO membrane|PEO|Li symmetric cell, which is among the best reported in the literature (Fig. 5c) [50–56]. Additionally, good galvanostatic cycling performance was also obtained owing to the uniform and dense structure made possible by our method (Fig. 5d). These results suggest that our technique can indeed benefit a variety of solid Li^+ conductors.

Conclusion

In conclusion, we have demonstrated a universal method for the synthesis of high-quality, high-performance solid-state electrolyte membranes. The approach is enabled by Joule heating of carbon heaters that can provide a higher temperature and shorter processing time compared to conventional sintering. The high temperature can effectively remove impurities to improve densification, and therefore the electrochemical performance. This rapid sintering prevents the loss of Li, as well as the deformation of the membrane, and most importantly offers fine control over the grain growth (*i.e.*, grain size and distribution). Using LLZTO (garnet) and LLTO (perovskite) as model materials, we show that highly dense and uniform solid-state electrolyte membranes can be synthesized in just 30 s at 1500 K. The resulting membranes demonstrate excellent electrochemical performance in terms of high conductivity and good stability in comparison with the literature. This study paves a new way to synthesize a variety of solid-state electrolyte membranes for the next generation of safe and high-performance batteries.

Materials and methods

Starting materials

The $Li_{6.5}La_3Zr_{1.45}Ta_{0.55}O_{12}$ garnet calcined powders were synthesized via solid-state reaction as reported previously [57]. In brief,

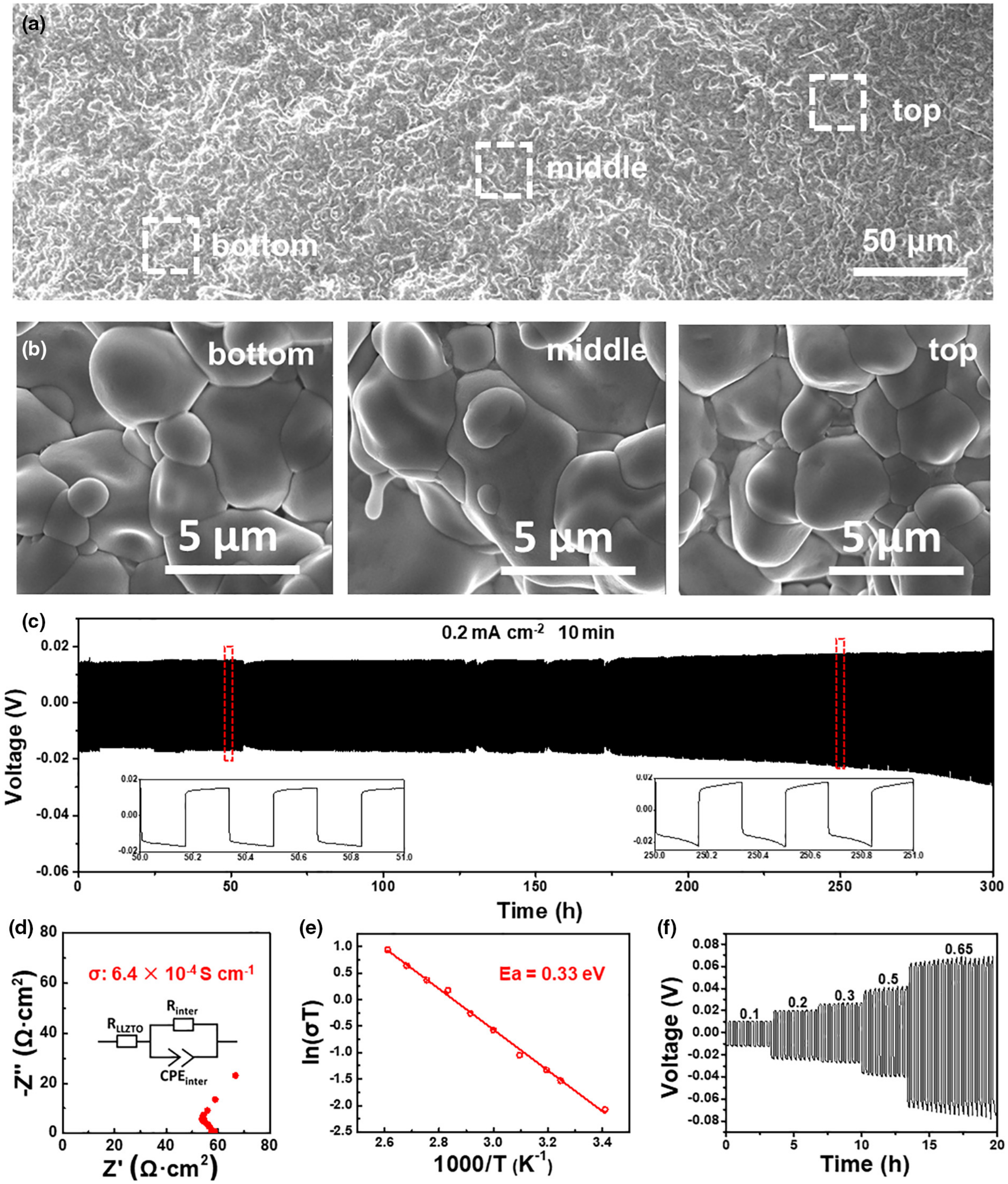

FIGURE 4

(a) SEM image showcasing the surface microstructure of the LLZTO membrane. (b) SEM images of the LLZTO membrane at three representative spots from the surface. (c) Galvanostatic cycling test of the LLZTO membrane using a Li|LLZTO membrane|Li symmetric cell configuration. The (d) ionic conductivity, (e) E_a, and (f) rate performance of the LLZTO membrane, measured in a Li|LLZTO membrane|Li symmetric cell configuration.

precursors including $LiOH{\cdot}H_2O$ (99.9%, Sigma-Aldrich), La_2O_3 (≥99.9%, Sigma-Aldrich), ZrO_2 (99.9%, Sigma-Aldrich), and Ta_2O_5 (99.9%, Sigma-Aldrich) were mixed at stoichiometric amounts and ball milled using isopropyl alcohol (IPA) for 12 h. A 10% excess of $LiOH{\cdot}H_2O$ was added to compensate for the loss of lithium during the sintering processes. Al_2O_3 nanopowder (~1 wt% of the total material) was added to assist in the sintering process. The resulting powders were calcined at 1193 K for 12 h. The obtained powders were then pressed into pellets at 300 MPa with a diameter of 8 mm and thickness of about 570 μm. The LLTO perovskite powders were synthesized according to literature, then pressed to pellets in the same manner [54].

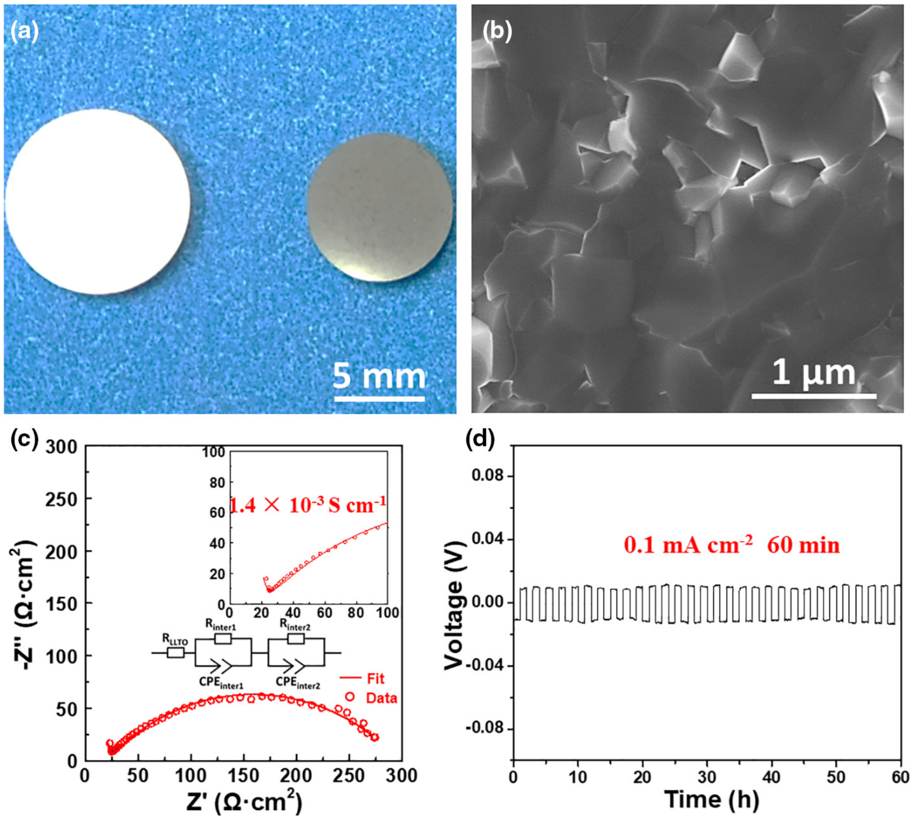

FIGURE 5

(a) Digital image comparing the LLTO membrane before (left) and after (right) the high-temperature rapid sintering process. (b) Fractured cross-sectional SEM image of the LLTO membrane after the high-temperature rapid sintering process. (c) Ionic conductivity of the LLTO membrane measured using a Li|PEO|LLTO membrane|PEO|Li symmetric cell configuration at 298 K. The red line indicates the fitted curve according to the equivalent circuit. (d) Galvanostatic cycling test of the LLTO membrane using a Li|PEO|LLTO membrane|PEO|Li symmetric cell configuration at 0.1 mA cm^{-2}.

Nitrate salts precursors of $LiNO_3$, $La(NO_3)_3{\cdot}6H_2O$ and citric acid were dissolved into deionized water with a stoichiometry of $Li_{0.35}La_{0.55}TiO_3$, followed by blending with a mixture solution of titanium isopropoxide and ethylene glycol to form the LLTO sol. An additional 20 mol% $LiNO_3$ was added to compensate for lithium loss. After being gelated at 70 °C for 12 h and dried at 100 °C, the sol transformed to a brown resin. Finally, the LLTO powder was obtained by calcining the resin at 350 °C for 6 h and 750 °C for 3 h.

High-temperature synthesis

Two pieces of carbon felt (Fuel Cell Earth) were attached to the edge of a glass substrate using silver paste, as described previously [58]. A DC power supply (StarPower, 0 ~100 V, 0 ~50 A) was used for the high temperature sintering. The carbon felt (Fuel Cell Earth, 10 × 1.5 cm) was connected with the DC power supply as the Joule heating element. The pressed LLZTO/LLTO pellets was placed on the heater. The voltage was ramped up to 28 V immediately by turning the voltage knob where the current was about 25 A. The high-temperature were conducted in an argon-filled glovebox with oxygen content below 2 ppm. The high-temperature heating process was recorded using a digital camera (Canon 60D, 30 frames s^{-1}). The light emission from the carbon felt was collected by a visible-near-infrared spectrometer (USB2000+, Ocean Optics), then calculated by fitting the radiation spectrum as reported previously [59].

Materials characterization

The surface and fractured cross-sectional morphologies of the membranes before and after sintering were observed using a Tescan GAIA Plasma FIB/SEM. XRD was performed on a D8 Bruker Advanced XRD system using a Cu Kα radiation source operated at 40 kV and 40 mA.

Electrochemical measurements

The synthesized LLZTO solid state electrolyte membrane was coated with Li metal on both sides using a method reported previously [60]. Electrochemical measurements of the Li|LLZTO membrane|Li symmetric cell were tested using a BioLogic VMP3 potentiostat at room temperature. EIS was performed using a frequency range of 100 mHz to 1 MHz with 20 mV AC amplitude. The ionic conductivity of the electrolyte was calculated by the equation $\sigma = D/(A * R)$, where D, A, and R refer to the thickness, area, and resistance, respectively. Galvanostatic stripping/plating of the Li|LLZTO membrane|Li symmetric cell was performed with a series of current densities at ambient condition; each step was carried for 10 min. The Li|PEO|LLTO membrane|PEO|Li symmetric cell was constructed as follows. First, polyethylene oxide (PEO, Mw = 800 000, Sigma-Aldrich) and Lithium bis(trifluoromethanesulfonyl)imide (Adamas) were dissolved into acetonitrile with an EO/Li ratio of 15. Then the solution was dropped on to both LLTO surfaces and dried for 2 h. Li films were then adhered to both sides of LLTO membrane. Galvanostatic stripping/plating of the Li|PEO|LLTO membrane|PEO|Li symmetric cell was performed at 0.1 mA cm^{-2} at ambient condition; each step was carried out for 60 min. All electrochemical measurements were conducted in an argon-filled glovebox.

CRediT authorship contribution statement

Min Hong: Conceptualization, Methodology, Investigation, Writing - review & editing. **Qi Dong:** Investigation, Supervision, Writing - review & editing. **Hua Xie:** Methodology, Investigation. **Xizheng Wang:** Methodology, Investigation. **Alexandra H. Brozena:** Writing - review & editing. **Jinlong Gao:** Methodology, Investigation. **Chengwei Wang:** Methodology. **Chaoji Chen:** Writing - review & editing. **Jiancun Rao:** Investigation. **Jian Luo:** Writing - review & editing. **Liangbing Hu:** Conceptualization, Writing - review & editing, Supervision.

Declaration of Competing Interest

The authors declare that they have no known competing financial interests or personal relationships that could have appeared to influence the work reported in this paper.

Acknowledgements

This work is not directly funded. The authors gratefully acknowledge the Maryland NanoCenter, the Surface Analysis Center, and the AIMLab.

Author contributions

L.H. conceived the idea. M.H. and Q.D. designed the experiments. M.H. and H.X. carried out most of the experiment. H.X. and J.G. collected the digital images. X.W. calibrated the temperature profile for the sintering device. C.W. designed the Joule heating device. M.H., Q.D., and C.C. designed the figures. M.H. and Q.D. collectively wrote the paper with input from all authors. A.H.B. revised the manuscript. J.L. analyzed the grain growth mechanism. L.H. supervised the project. All authors discussed the results and contributed to the final manuscript.

Data and materials availability

All data are available in the manuscript and the supporting materials.

Appendix A. Supplementary data

Supplementary data to this article can be found online at https://doi.org/10.1016/j.mattod.2020.10.002.

References

[1] M. Li et al., Chem. Rev. 120 (2020) 6783–6819.
[2] A. Manthiram, X. Yu, S. Wang, Nat. Rev. Mater. 2 (2017) 16103.
[3] T. Famprikis et al., Nat. Mater. 18 (2019) 1278–1291.
[4] Y. Jin et al., Nat. Energy 3 (2018) 732–738.
[5] Q. Zhang et al., Adv. Mater. 31 (2019) 1901131.
[6] G. Hitz et al., Mater. Today 22 (2019) 50–57.
[7] T. Swamy et al., J. Electrochem. Soc. 165 (2018) A3648–A3655.
[8] J. Duan et al., Adv. Fund. Mater. 30 (2020) 1908701.
[9] X. Huang et al., J. Materiomics 5 (2019) 221–228.
[10] X. Zeng et al., J. Storage Mater. 27 (2020) 101128.
[11] X. Huang et al., Energy Storage Mater. 22 (2019) 207–217.
[12] M. Dixit et al., ACS Appl. Mater. Interfaces 11 (2019) 2022–2030.
[13] H. Huo et al., Nano Energy 73 (2020) 104836.
[14] H. Yamada, T. Ito, R. Basappa, Electrochim. Acta 222 (2016) 648–656.
[15] K. Kataoka, H. Nagata, J. Akimoto, Sci. Rep. 8 (2018) 9965.
[16] L. Cheng et al., ACS Appl. Mater. Interfaces 7 (2015) 17649–17655.
[17] F. Aguesse et al., ACS Appl. Mater. Interfaces 9 (2017) 3808–3816.
[18] Y. Ren et al., Electrochem. Commun. 57 (2015) 27–30.
[19] Y. Ren et al., ACS Appl. Mater. Interfaces 11 (2019) 5928–5937.
[20] L. Cheng et al., J. Mater. Chem. A 2 (2014) 172–181.
[21] C. Li et al., J. Alloy. Compd. 695 (2017) 3744–3752.
[22] R. Basappa et al., J. Power Sources 363 (2017) 145–152.
[23] W. Jr et al., J. Power Sources 412 (2019) 287–293.
[24] S. Ramakumar et al., Prog. Mater. Sci. 88 (2017) 325–411.
[25] H. Li et al., Ceram. Int. 45 (2019) 18115–18118.
[26] L. Chen et al., ACS Appl. Mater. Interfaces 7 (2015) 2073–2081.
[27] M. Botros et al., J. Power Sources 309 (2016) 108–115.
[28] J. Sakamoto et al., Nanotechnology 24 (2013) 424005.
[29] J. Gai et al., J. Eur. Ceram. Soc. 38 (2018) 1673–1678.
[30] R. Shin et al., Solid State Ionics 301 (2017) 10–14.
[31] E. Yi et al., ACS Appl. Energy Mater. 3 (2020) 170–175.
[32] M. Badding, X. Liu, Y. Lu, Stabilized solid garnet electrolyte and methods thereof. U. S. Patent 10211481B2, 2019..
[33] E. Hanc et al., J. Solid State Chem. 248 (2017) 51–60.
[34] C. Wang et al., Energy Storage Mater. 17 (2019) 234–241.
[35] F. Li, J. Pan, Modelling “nano-effects” in sintering, in: R. Castro, K. van Benthem (Eds.), Sintering. Engineering Materials, Springer, Berlin, Heidelberg, 2012.
[36] Z. Fang, H. Wang, Int. Mater. Rev. 53 (2008) 326–352.
[37] F. Wakai, M. Yoshida, B. Kashyap, J. Ceram. Soc. Jpn. 114 (2006) 974–978.
[38] H. Wang, Z. Fang, K. Hwang, Metall. Mater. Trans., A 42 (2011) 3534–3542.
[39] M. Rawlence et al., Nanoscale 8 (2016) 14746–14753.
[40] J. Su et al., Ceram. Int. 45 (2019) 14991–14996.
[41] S. Yu et al., Chem. Mater. 28 (2016) 197–206.
[42] L. Yang et al., Ceram. Int. 46 (2020) 10917–10924.
[43] Y. Zhang et al., J. Power Sources 268 (2014) 960–964.
[44] J. Lin et al., J. Energy Chem. 40 (2020) 132–136.
[45] B. Xu et al., J. Power Sources 302 (2016) 291–297.
[46] K. Ishiguro et al., J. Electrochem. Soc. 161 (2014) A668.
[47] S. Zhang et al., Chem. Eng. J. 393 (2020) 124797.
[48] Y. Li et al., J. Am. Chem. Soc. 140 (2018) 6448–6455.
[49] B. Liu et al., Nano Lett. 17 (2017) 4917–4923.
[50] A. Belous et al., Russ. J. Electrochem. 50 (2014) 523–530.
[51] D. Lakshmi et al., J. Mater. Sci.: Mater. Electron. 31 (2020) 1343–1354.
[52] M. Ling et al., Ionics 22 (2016) 2151–2156.
[53] W. Kwon et al., J. Mater. Chem. A 5 (2017) 6257.
[54] H. Le et al., Electrochim. Acta 248 (2017) 232–242.
[55] Z. Hu et al., New J. Chem. 42 (2018) 9074.
[56] V. Avila et al., Scr. Mater.. 176 (2020) 78–82.
[57] H. Xie et al., ACS Energy Lett. 4 (2019) 2668–2674.
[58] C. Wang et al., Science 368 (2020) 521–526.
[59] X. Wang et al., Adv. Mater. (2020) 2002853.
[60] X. Han et al., Nat. Mater. 16 (2017) 572–579.